



Cite this: *RSC Adv.*, 2021, **11**, 39455

The dolabellane diterpenes as potential inhibitors of the SARS-CoV-2 main protease: molecular insight of the inhibitory mechanism through computational studies†

Nanik Siti Aminah,^{id *ab} Muhammad Ikhlas Abdjan,^{ac} Andika Pramudya Wardana,^{ac} Alfinda Novi Kristanti,^{ab} Imam Siswanto,^{ad} Khusna Arif Rakhman^e and Yoshiaki Takaya^f

An investigation has been carried out on natural products from dolabellane derivatives to understand their potential in inhibiting the SARS-CoV-2 main protease ($3CL^{Pro}$) using an *in silico* approach. Inhibition of the $3CL^{Pro}$ enzyme is a promising target in stopping the replication of the SARS-CoV-2 virus through inhibition of the subsite binding pocket. The redocking process aims to determine the $3CL^{Pro}$ active sites. The redocking requirement showed a good pose with an RMSD value of 1.39 Å. The combination of molecular docking and MD simulation shows the results of DD13 as a candidate which had a good binding affinity (kcal mol⁻¹) to inhibit the $3CL^{Pro}$ enzyme activity. Prediction of binding free energy (kcal mol⁻¹) of DD13 using the Molecular Mechanics-Poisson Boltzmann/Generalized Born Surface Area (MM-PB/GBSA) approach shows the results $\Delta G_{bind(MM-GBSA)}$: -52.33 ± 0.34 and $\Delta G_{bind(MM-PBSA)}$: -43.52 ± 0.42 . The key residues responsible for the inhibition mechanism are His41, Ser46, Met49, Asn142, Cys145, His163, Met165, and Gln189. Additionally, pharmacokinetic prediction recommended that DD13 had promising criteria as a drug candidate. The results demonstrated in this study provide theoretical information to obtain a potential inhibitor against the SARS-CoV-2 main protease.

Received 14th October 2021
 Accepted 30th November 2021

DOI: 10.1039/d1ra07584e
rsc.li/rsc-advances

Introduction

Coronavirus disease 2019 (COVID-19) is a pandemic that has been going on since 2019. The disease is caused by acute respiratory syndrome coronavirus 2 (SARS-CoV-2).^{1,2} In general, the coronaviruses are positive-sense single-stranded RNA viruses in the coronavirus genus.^{2,3} The coronavirus has multiple open reading frames (ORF), such as ORF1 and ORF2. These frames are responsible for producing the two polypeptides pp1a and pp1ab.^{4,5} Then, these polypeptides are processed by the main protease or 3C-like protease (M^{Pro} or $3CL^{Pro}$), which is responsible for the coronavirus replication cycle.^{6,7}

Therefore, the main protease SARS-CoV-2 becomes a promising target of COVID-19 disease drug development.^{7,8}

Structurally, the SARS-CoV-2 main protease has three domains, such as domain I (residues 10–99), domain II (residues 100–184), and domain III (residues 201–300) (Fig. 1A). Additionally, residue 185–200 is a long loop region that connects domain I and domain II.⁹ More specifically, the subsite binding pocket SARS-CoV-2 main protease contains His41 and Cys145 residues, which play a crucial role as catalysis centers.¹⁰ Mutations that occurred in amino acid residues for the main proteases of SARS-CoV-2 and SARS-CoV showed a similarity percentage of 83% with 12 amino acid residue mutations in each sequence (residue number: 35, 46, 65, 86, 88, 94, 134, 180, 202, 267, 285, and 286).^{11,12} It had been reported, the mutation of the Ser46 amino acid residue causes a conformational change in the subsite binding pocket of SARS-CoV-2 main protease.¹³ These changes can increase the surface area and volume in the subsite binding pocket of SARS-CoV-2 main protease. It is the main focus variable needed to understand because the subsite binding pocket plays a crucial role in the inhibitory mechanism of SARS-CoV-2 main protease.¹⁴ Studies on the interaction of inhibitors with amino acid residues in the subsite binding pocket are expected to be a solution to increase the development possibility of SARS-CoV-2 main protease inhibitors.

^aDepartment of Chemistry, Faculty of Science and Technology, Universitas Airlangga, Surabaya 60115, Indonesia. E-mail: nanik-s-a@fst.unair.ac.id

^bBiotechnology of Tropical Medicinal Plants Research Group, Universitas Airlangga, Indonesia

^cPh.D. Student of Mathematics and Natural Sciences, Faculty of Science and Technology, Universitas Airlangga, Komplek Kampus C UNAIR, Jl. Mulyorejo, 60115, Surabaya, Indonesia

^dBioinformatic Laboratory, UCoE Research Center for Bio-Molecule Engineering, Universitas Airlangga, Surabaya, Indonesia

^eDepartment of Chemistry Education, Universitas Khairun, Ternate, Indonesia

^fFaculty of Pharmacy, Meijo University, Nagoya, Japan

† Electronic supplementary information (ESI) available. See DOI: 10.1039/d1ra07584e



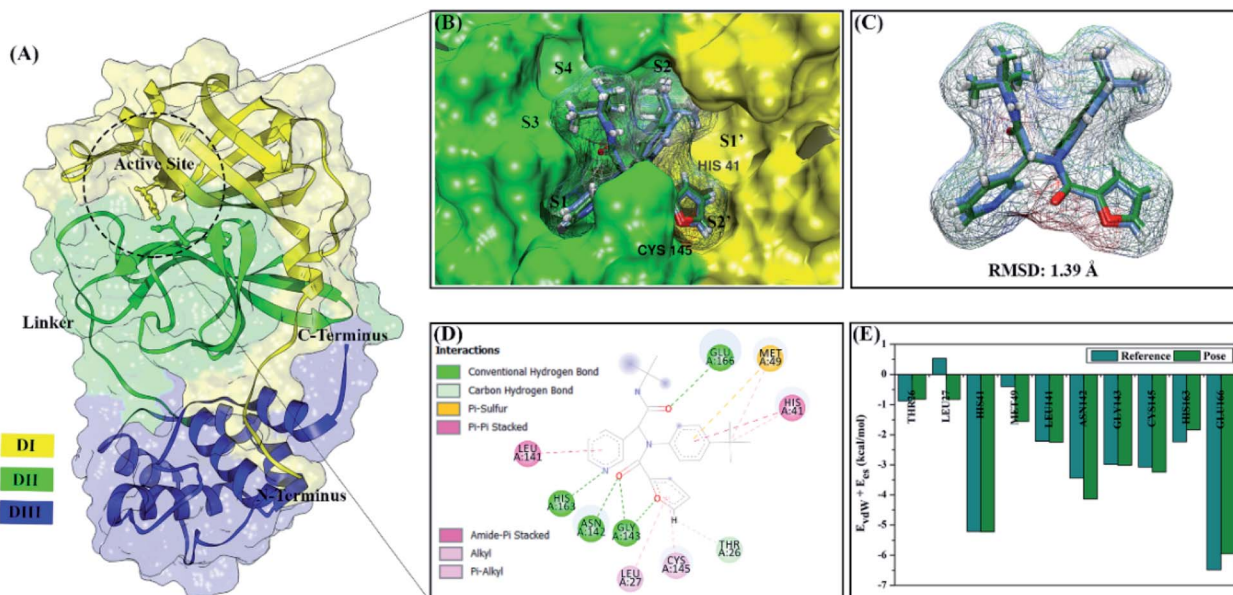


Fig. 1 Redocking stage: (A) the structure of main protease SARS-CoV-2, (B) active site of $3CL^{pro}$ with subsites labelled, (C) ligand native superposition represented by crystal (cornflower blue) and flexible conformation (forest green), (D) the interaction types of the 0EN– $3CL^{pro}$ show in 2D-diagram, and (E) the footprint energy of key binding residues.

The development of SARS-CoV-2 main protease inhibitors was reported by several previous studies.^{15,16} One of them is the compound ML188, which has an inhibitory activity of the $3CL^{pro}$ enzyme with an IC_{50} value of $2.5 \mu\text{M}$.¹² Besides, several reports state that natural product compounds have potential as SARS-CoV-2 main protease inhibitor.^{17–20} Some of them that have been reported are diterpene derivatives that have the inhibitor activity of SARS-CoV main protease.²¹ The report provides information that the diterpene derivative has the potential to inhibit the main protease of SARS-CoV-2. Several works of literature give similar recommendations about the potential of diterpenes as a promising SARS-CoV-2 main protease inhibitor.^{19,20} The selection of inhibitor candidates from natural products is starting with the consideration that compounds already have biological activity against some diseases or infections.²² The dolabellane (subclass diterpene) can be isolated from *Caribbean Eunicea laciniata*²³ and *Nigella damascena*.²⁴ These compounds are the main focus to investigate their potential as candidate inhibitors in this study. Some research reported dolabellane compounds had potential as antivirals.^{20,24,25} Hopefully, this research can provide information about the potential of dolabellane derivatives as inhibitors against the main protease SARS-CoV-2.

Theoretical studies using *in silico* approach provide another alternative in finding candidate compounds that have potential as main protease inhibitors of SARS-CoV-2.^{26–28} The combination of molecular docking and Molecular Dynamic (MD) simulation provides a comprehensive, structure-based approach in studying the interaction of inhibitors with the SARS-CoV-2 main protease at the molecular level.^{11,22} Several previous studies have offered an MD simulation approach for M^{pro} or $3CL^{pro}$ enzymes to study their conformational dynamics.^{22,29–31} In particular, the

interaction of the inhibitor with amino acid residues at the subsite binding pocket. Additionally, structure-based studies can provide a more detailed description of the inhibition mechanism through interactions with residues of the catalytic centre (His41 and Cys145), which regulate the replication of the COVID-19 virus.^{10,13} An important variable that is considered in this study is binding free energy (ΔG_{bind}) to predict the inhibitor–receptor binding affinity. It is a crucial point to evaluate the criteria for a promising inhibitor of SARS-CoV-2 main protease. Besides, pharmacokinetic studies are expected to provide initial information of selected inhibitors as drug candidates that meet the criteria.

Methodology

Inhibitor and protein preparation

The selection of a target protein using co-crystal SARS-CoV-2 main protease ($3CL^{pro}$) from the protein data bank (PDB ID: 7L0D). The complex crystal contains a native ligand (PDB ID: 0EN), namely *N*–[(1*R*)-2-(*tert*-butylamino)-2-oxo-1-(pyridine-3-yl)ethyl]-*N*–(4–*tert*-butylphenyl)furan-2-carboxamide or ML188 on the active site of the $3CL^{pro}$ enzyme as a non-covalent inhibitor. The ML188 (0EN) ligand was a reference in this study because it has known as an inhibitor of the $3CL^{pro}$ enzyme.¹² ML188 inhibitor coordinates and amino acid residues (receptors) were extracted from the crystal structure $3CL^{pro}$ using the Chimera version 1.13 package for docking and MD simulation purposes. Meanwhile, the candidate ligands used in this study were 14 diterpene derivatives (Fig. S1†) of the dolabellane type obtained from the literature review.²⁰ Calculation of electrostatic potential (ESP) charges for candidate ligands uses the Semiempirical Quantum Parametric Method-3 (SQM-PM3) contained in the



Gaussian 16 package.³² The AMBER FF14SB force field and Austin Model 1-bond charge correction are needed to calculate coordinate parameters of ligand and receptor.

Molecular docking

The molecular docking study involves two stages: (i) the redocking process and (ii) docking candidate ligands through the DOCK6 package. The redocking process aims to determine the coordinates of the active site of the 3CL^{pro} enzyme based on the selected sphere (a radius 10 Å from the 0EN coordinate). The scoring function based on the grid score function with the grid spacing used is 0.3 Å. The minimization process aims to minimize energy in each system. The redocking criteria evaluate through the best pose with RMSD criteria 2.0 Å.^{33,34} The footprint analysis was carried out to investigate the interaction between native ligands and amino acid residues on the active site. The redocking process that meets the criteria is used as the initial coordinate for the candidate docking process. The flexible conformational type is used in molecular docking to determine the interaction between the inhibitor and 3CL^{pro} in the gas phase.

Molecular dynamics simulation

Topology preparation (ligand, receptor, receptor-solvated, complex, and complex-solvated) on each system using tleap tools in the AMBER18 package. The application of the general AMBER force field (GAFF) to each ligand is used as the initial coordinates for the topology preparation of each system.³⁵ These coordinates are the integration of the score function from the molecular docking results. Especially in receptor-solvated topology, it aims to see the dynamical conformation of the 3CL^{pro} enzyme without the influence of inhibitors that bind to the active site. The solvent model used is TIP3P water solvent using a minimum distance of 12 Å. The ion neutralizing system used is the sodium ions (Na⁺) randomly added. The water molecules were minimized by 500 steps of steepest descent and 1500 steps of conjugated gradient, while the rest of the atoms were restrained. Then, the receptor and ligand were minimized by 500 steps of steepest descent and 1500 steps of the conjugated gradient with the restrained solvent. In the last step of minimization, the entire system was fully minimized by the same procedure.

The simulation process is carried out through several stages, such as heating, equilibrium, and production. The heating stage of the system uses a gradual heating step from 10 K to 310 K (200 ps) with a harmonic restraint of 30 kcal mol⁻¹ Å⁻². The equilibrium stage (1300 ps) for each system was carried out periodically through four steps with harmonic restraint of 30, 20, 10, and 5 kcal mol⁻¹ Å⁻². Finally, the entire system is simulated under the NPT ensemble (310 K and 1 atm) until reaching 100 ns. The production stage (0–100 ns) aims to produce trajectories for further analysis and evaluation.³⁶

Trajectories analysis

Trajectories analysis uses several tools available in the AMBER18 package for calculation purposes, such as processs mdout.perl and cpptraj tools. The overall analysis of trajectories (0–100 ns) aims to evaluate the stability of each system through

several variables, such as total energy and root-meant-square displacement (RMSD). Meanwhile, the analysis of other variables, such as flexibility, compactness, solvent accessibility, binding free energy, energy decomposition, atom contacts, hydrogen bonding uses the last 20 ns (80–100 ns) trajectories. This consideration is taken based on the efficiency of calculation time.³⁷ Besides, the trajectories used are trajectories that have achieved good stability. Its characterized by no significant fluctuations in the RMSD complex. To evaluate several variables such as percentage of atom contacts (P_{AC}) and percentage of hydrogen bonding (P_{HB}) can be calculated using eqn (1) and (2). The number of frames per H-bond or atom contact (N_{fra}) is divided by the total number of frames (N_{tot}) during the simulation time of 2000 frames.

$$P_{AC} = \left[\frac{N_{\text{fra}}}{N_{\text{tot}}} \right] \times 100\% \quad (1)$$

$$P_{HB} = \left[\frac{N_{\text{fra}}}{N_{\text{tot}}} \right] \times 100\% \quad (2)$$

Calculation of binding free energy (ΔG_{bind}) and energy decomposition ($\Delta G_{\text{bind}}^{\text{residue}}$) using the MMPBSA.py tools available in the AMBER18 package.³⁸ The binding free energy was calculated using the Molecular Mechanics-Poisson Boltzmann/Generalized Born Surface Area (MM-PB/GBSA) approach. Several key parameters were used for each approach: MM-GBSA (the generalized Born solvation model: 2, the concentration of mobile counterions in solution: 0.00 M, and nonpolar contribution of solvation free energy: 0.0072) and MM-PBSA (molecule dielectric constant: 1, solvent dielectric constant: 80.0, solvent probe radius: 1.4 Å, and nonpolar contribution of solvation free energy: 0.0072). Mathematically, binding free energy can be calculated using eqn (3). However, the entropy change ($-T\Delta S$) is ignored because of the high computational cost and low prediction accuracy.³⁹ Specifically, the energy components that affect binding free energy are described in the gas phase (eqn (4)) and the solvation phase (eqn (5)). Energy components in the gas phase show energy components consisting of bonded energy (ΔE_{bonded}), van der Waals energy (ΔE_{vdW}), and electrostatic energy (ΔE_{ele}). In particular, bonded energy identifies bond, angle, and torsion energies, which are assumed to have conformational energy equal to zero. Meanwhile, the solvent phase is the total of Poisson Boltzmann/generalized Born models ($\Delta G_{\text{sol}}^{\text{ele}}$) and solvent-accessible surface area energy ($\Delta G_{\text{sol}}^{\text{nonpolar}}$). The energy decomposition uses the MM-GBSA approach, which can be calculated completely using eqn (6).

$$\Delta G_{\text{bind}} = \Delta G_{\text{gas}} + \Delta G_{\text{solv}} - T\Delta S \quad (3)$$

$$\Delta G_{\text{gas}} = \Delta E_{\text{bonded}} + \Delta E_{\text{vdW}} + \Delta E_{\text{ele}} \quad (4)$$

$$\Delta G_{\text{sol}} = \Delta G_{\text{sol}}^{\text{ele}} + \Delta G_{\text{sol}}^{\text{nonpolar}} \quad (5)$$

$$\Delta G_{\text{bind}}^{\text{residue}} = \Delta E_{\text{vdW}} + \Delta G_{\text{sol(GB)}}^{\text{nonpolar}} + \Delta E_{\text{ele}} + \Delta G_{\text{sol(GB)}}^{\text{ele}} \quad (6)$$



ADMET calculation

The study of absorption, distribution, metabolism, excretion and toxicity (ADMET) is also studied to see the ability of the candidate's biological activity as a drug in the body. Prediction of these pharmacokinetic properties using the pkCSM web service, which can describe in detail the ADMET properties.⁴⁰

Results and discussion

Molecular docking study

All steps of molecular docking are performed by the DOCK6 package. The active site determination using initial coordinates of the native ligand (0EN) extracted from the crystal structure is based on a cluster sphere selection. The redocking process provides convenience and accuracy in determining the active site of the receptor.³³ Structurally, the active site of the 3CL^{pro} enzyme has His41 and Cys145 residues as catalytic centers located on the subsite binding pocket.¹⁰ The redocking results showed that the native ligand was docked very well to the active site of the receptor (Fig. 1B). The data is supported by the redocking results of the native ligand showing a good pose with an RMSD value of 1.39 Å and a grid score: $-72.58 \text{ kcal mol}^{-1}$ using a flexible conformation (Fig. 1C). This value explains that the pose ligand coordinates have coordinates that are close to the crystal coordinates. It can describe more the accuracy of the interaction between the ligand and amino acid residues on the 3CL^{pro} subsite binding pocket. In particular, the interaction of native ligands with amino acid residues on the subsite binding pocket, including S2' (Thr25 and Leu27), S2 (His41 and Met49), S1 (Leu141, Asn142, Gly143, Cys145, His163), and S3 (Glu166). These amino acid residues are the main amino acid

residue that responsible for the 0EN–3CL^{pro} interaction. Besides, the amino acid residues on the S1' and S4 binding subsites only show a van der Waals interaction. There are four residues, such as Asn142, Gly143, His163, and Glu166 responsible for hydrogen bonding interactions (Fig. 1D). Hydrogen bonding (H-bond) variables have a crucial role in explaining the inhibition mechanism of the 3CL^{pro} enzyme.^{14,22} The footprint analysis was showed on ten amino acid residues on the 3CL^{pro} active site. This variable was performed by comparing the van der Waals energy and electrostatic energy ($E_{\text{vdw}} + E_{\text{es}}$) ligand reference and pose in the gas phase (Fig. 1E). Overall, the redocking process showed good criteria in determining the active site of the 3CL^{pro} enzyme. However, these results need to be studied more comprehensively using molecular dynamic simulation (discussed in more detail below).

The coordinates and parameters obtained from the redocking results are used as the main reference in the docking candidate process. The optimized candidates docked into the active site of the 3CL^{pro} enzyme using a flexible conformation (Fig. 2A). The results show that two candidates have good interactions with 3CL^{pro}, such as DD9: $-72.66 \text{ kcal mol}^{-1}$ and DD13: $-74.53 \text{ kcal mol}^{-1}$ (Fig. 2B). This consideration is taken based on the grid score pose < grid score candidate. The lower value of the grid score shows better interaction with the receptor.⁴¹ Overall, the energy contribution (higher negativity value) is shown by E_{vdw} compared to E_{es} in the gas phase. The results of the candidate docking based on the grid score function are described in detail in Table S1.[†]

The inhibitory mechanism of candidate against the 3CL^{pro} enzyme was studied through the interaction of amino acid residues on the subsite binding pocket.⁴² Each candidate shows

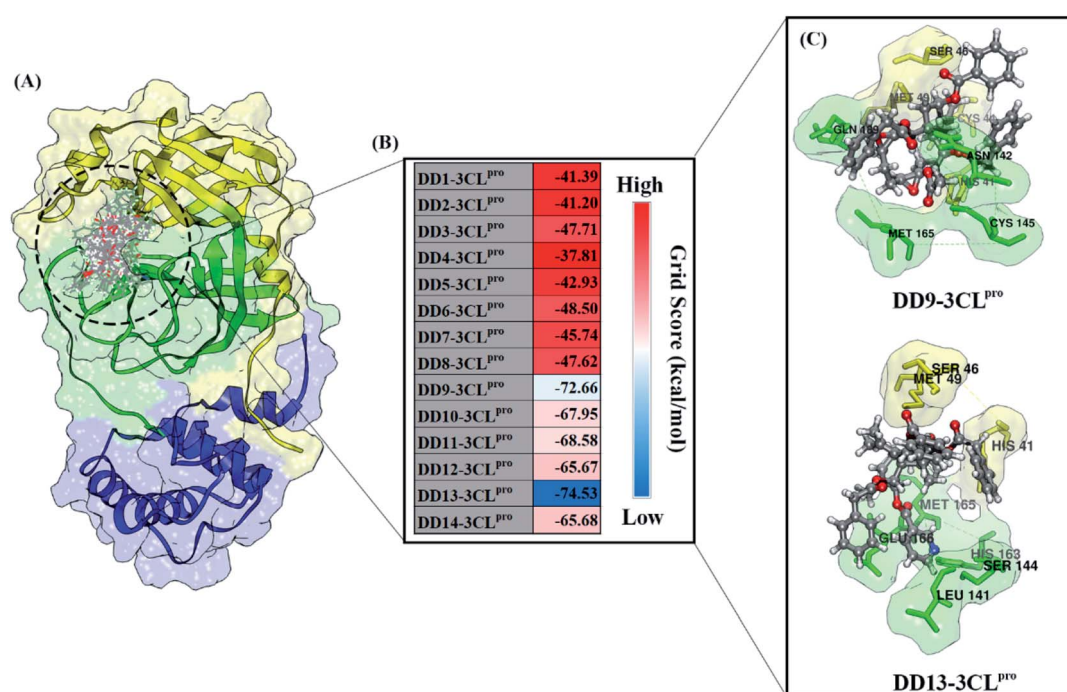


Fig. 2 Molecular docking analysis: (A) candidates–3CL^{pro} interaction in the active site, (B) heat map of grid score, and (C) selected candidates based on lowest grid score value.



that there are amino acid residues responsible for the inhibitor-receptor interaction: DD9-3CL^{pro} (His41, Cys44, Ser46, Met49, Asn142, Cys145, Met165, and Gln189) and DD9-3CL^{pro} (His41, Ser46, Met49, Leu141, Ser144, His163, Met165, and Glu166) (Fig. 2C). Specifically, there are residues responsible for H-bond interactions with each candidate ligand, including DD9-3CL^{pro} (Ser46, Cys146, Asn142, and Gln189) and DD13-3CL^{pro} (Ser46, His163, and Glu166) (Fig. S2†). These results provide a good initial image in understanding the interaction of key residues at the molecular level. Molecular docking studies are effective in obtaining the initial coordinates through relatively fast calculations. It aims to facilitate the process of further analysis using MD simulation.

Conformational dynamic study: stability, compactness, and flexibility of each system

The quality of the conformational dynamics of each system is evaluated through several variables, such as stability,^{11,43} compactness,⁴⁴ and flexibility.^{45,46} The calculation of the root-mean-square deviation (RMSD) aims to determine the stability of each system in the form of complex, backbone, and ligand RMSD (Fig. 3). Notably, the all atoms RMSD did not show any significant fluctuation in the last 20 ns of trajectories (80–100 ns). Additionally, each complex showed similar fluctuations with the apo protein (3CL^{pro} enzyme). This data is reinforced by the average value of all atoms RMSD (nm), which is relatively the same for each system: 3CL^{pro}: 0.25 ± 0.04, 0EN-3CL^{pro}: 0.26 ±

0.04, DD9-3CL^{pro}: 0.26 ± 0.04, and DD13-3CL^{pro}: 0.27 ± 0.04. These results describe that the level of stability in each complex (inhibitor-3CL^{pro}) showed good results. The presence of an inhibitor on the 3CL^{pro} active site did not give a significant change in the 3CL^{pro} structure. It becomes an important parameter in evaluating other variables. Good system stability will provide a clear image of the interaction between the inhibitor and the 3CL^{pro} enzyme. The same fluctuation is also shown by the average value of the backbone and ligand RMSD (Table S2†). The total energy analysis was carried out to see the system stability from the thermodynamic aspect (Fig. S3†). The data shows that each system has converged and has not experienced excessive fluctuations (Table S2†). The stability achieved in each system, especially in the last 20 ns trajectories, was used for further analysis purposes.^{11,37}

The radius of gyration (RoG) analysis aims to obtain more information about equilibrium conformation and structure compactness during the last 20 ns of simulation.³⁷ The results show that each system has a relatively compact structure with insignificant fluctuation (~2.23 nm) (Fig. S4†). It is further strengthened by the average value of RoG on Apo protein (without inhibitor) and complex (with inhibitor) (Table S2†). Additionally, the results of the RoG analysis also show that each system has a stable folded structure.

The root-mean-square fluctuation (RMSF) and B-factor calculation aim to see the flexibility of each system.^{46,47} The DD13-3CL^{pro} complex showed significant RMSF and B-factor fluctuations compared to 3CL^{pro}, 0EN-3CL^{pro}, and DD9-3CL^{pro} (Fig. S5†). In contrast, Apo protein (3CL^{pro}) has a more rigid structure because it has lower fluctuations. Overall, the flexibility for each system is 3CL^{pro} > 0EN-3CL^{pro}, and DD9-3CL^{pro} (Table S2†). Meanwhile, an explanation of the fluctuations that occur in each system is found in the DI loop region (47–53, 60–62, 92) and DIII (215–222 and 274–280). However, overall there was no significant conformational change during the simulation time for each structure (Fig. 4). Especially in the

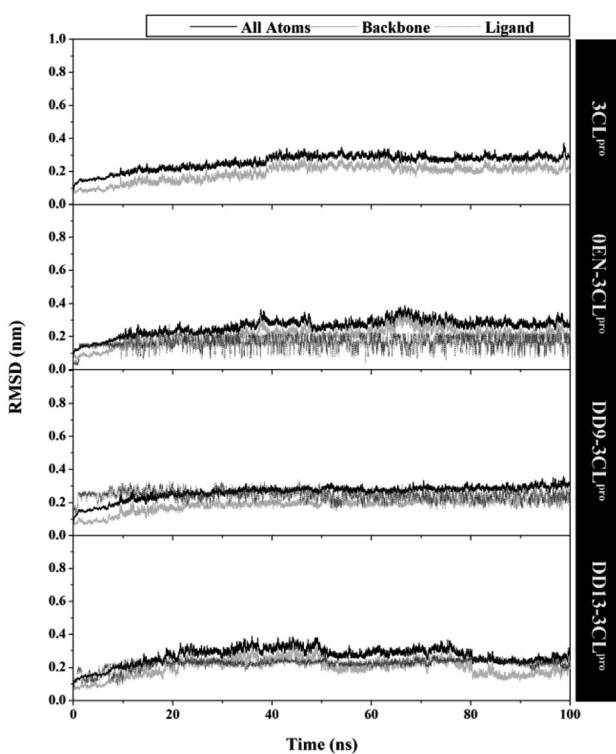


Fig. 3 The root-mean-square displacement of all atoms, backbone ($\text{C}\alpha$, C, N, and O), and ligand for each system plotted along the 100 ns of MD simulation.

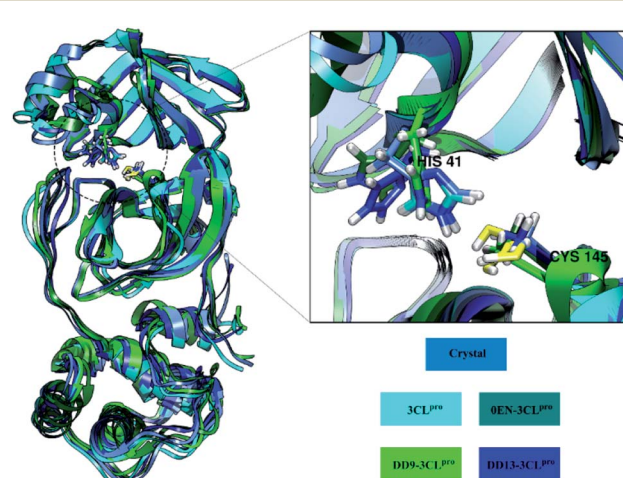


Fig. 4 Average structure of amino acid residues: each structure (3CL^{pro}, 0EN-3CL^{pro}, DD9-3CL^{pro}, and DD13-3CL^{pro}) extract from the last 20 ns trajectories. The structure fitted based on crystal structure as initial coordinate.



backbone (C α , C, N, and O), fluctuations show that the average structure has coordinates that are similar to the crystal structure. It indicates that the conformational flexibility of the structure in each system is quite stable during the simulation time. This data is supported by the stability of the complex RMSD and backbone RMSD at the last 20 ns simulation (Fig. 4). It should be noted, the high structural flexibility leads to high conformational complexity. More specifically, flexibility at the enzyme active site may play a crucial role in the potential binding of the inhibitor.³⁰ Therefore, it is necessary to carry out a more in-depth analysis of the key residues on the 3CL^{pro} active site. It aims to see the flexibility of the key residues, especially residues His41 and Cys145. The RMSF residues of His41 and Cys145 on the active site were investigated to see the fluctuation of the two residues as a catalytic centre. The results showed that the RMSF (nm) of the two residues for each structure: 3CL^{pro} (His41: ~0.30, Cys145: ~0.17), 0EN-3CL^{pro} (His41: ~0.48, Cys145: ~0.30), DD9-3CL^{pro} (His41: ~0.39, Cys145: ~0.28), and DD13-3CL^{pro} (His41: ~0.55, Cys145: ~0.29). The comparison of coordinates (His41 and Cys145 residues) between each system with the initial coordinates of the crystal structure shows that there are differences in conformation. It is possible because along the last 20 ns simulation, there is an interaction with the inhibitor that affects the force field (steric) on the two residues. Additionally, it could be caused by the presence of a water molecule on the 3CL^{pro} active site, which affects the dynamic conformation of each system.^{13,48} Hopefully, the study on the conformation dynamics of each system during the simulation can explain the interaction of inhibitor-3CL^{pro} at the molecular level.

Solvent accessibility of inhibitor-3CL^{pro} enzyme

The simulation process considers the solvent phase (water molecules) as a parameter that plays an important role in mediating the interaction of the inhibitor with the 3CL^{pro} enzyme.^{48,49} Based on the previous section, the influence of water molecules plays an important role in influencing the interaction of inhibitors with amino acids residue on the active site. Solvent accessibility surface area (SASA) is one of the variables that can describe the water's ability to access all surface and active site surfaces during the simulation time (Fig. 5). Overall, the access capability on the entire surface shows that each system has a value of all surface $> \sim 140.00 \text{ nm}^2$ (DD9-3CL^{pro} $>$ 3CL^{pro} $>$ DD13-3CL^{pro} $>$ 0EN-3CL^{pro}) and active site $> \sim 9.00 \text{ nm}^2$ (DD9-3CL^{pro} $>$ DD13-3CL^{pro} $>$ 3CL^{pro} $>$ 0EN-3CL^{pro}). Especially the SASA of the active site (radius 5 Å) is the main focus. The candidate ligands are more accessible to water solvent than Apo protein and native ligands based on the average SASA value of each system (Table S2†).

The fluctuation of the key residues on the enzyme active site causes a water molecule traffic that is important for maintaining protein structure.³⁰ Additionally, the effect of water molecules causes the stability of the protein structure to increase through the interaction of hydrogen bonds, salt bridges, and π - π stacking.^{31,50} It affects the conformation of the inhibitor at the active site of the 3CL^{pro} enzyme. The presence of water

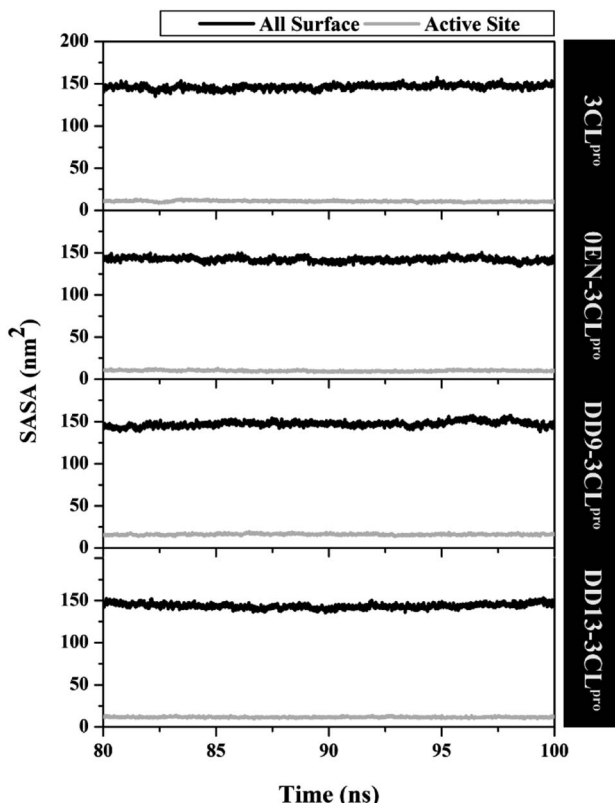


Fig. 5 The solvent-accessible surface area using the last 20 ns trajectories. A radius of 5 Å was used to calculate the SASA in the active site of each system.

molecules on the enzyme active site provides more opportunities to interact with the inhibitor interface. It is necessary to analyse the water molecules when approaching the inhibitor during the simulation.

The water molecules close to the inhibitor heteroatoms (O and N) in each complex are evaluated through the radial distribution function (RDF).¹¹ The analysis of this variable was performed based on the assumption that the inhibitor present on the active site of the complex could interact directly with water molecules. To test the RDF value, it can be shown by the integration number on the first minimum value of heteroatoms in each inhibitor.⁵¹ The 0EN-3CL^{pro} complex showed that the N2 atom in the first peak at a distance of ~0.3 nm had relatively high access to water molecules. In contrast, the rest of the heteroatoms in the 0EN-3CL^{pro} complex (N1, N3, O1, O2, and O3) suggest low water molecule access to these atoms (Fig. S6†). Meanwhile, the DD9-3CL^{pro} complex showed atoms O15, O19, O26, O32, and O35 (the first peak was consistent at the distance: ~0.27 nm) having relatively high access of water molecules on the active site compared to the rest of the atoms, such as O16, O18, O20, O21, and O30 (Fig. S7†). On the other hand, the DD13-3CL^{pro} complex showed atoms O25, O27, and O54 O35 (the first peak was consistent at a distance: ~0.27 nm) having relatively high access of water molecules on the active site compared to the rest of the atoms O15, O16, O18, O19, O20, O30, and N59 (Fig. S8†). Finally, we can assume that the



Table 1 Determination of energy component (kcal mol^{-1}) of the inhibitor– 3CL^{pro} enzyme using MM-PB/GBSA approach. Data are shown as mean \pm standard error of the mean (SEM)

Energy component	0EN– 3CL^{pro}	DD9– 3CL^{pro}	DD13– 3CL^{pro}
Gas phases			
E_{vdW}	-47.15 ± 0.22	-43.40 ± 0.29	-67.80 ± 0.31
E_{elec}	-35.22 ± 0.41	-8.34 ± 0.35	-32.03 ± 0.39
ΔG_{gas}	-82.37 ± 0.42	-51.75 ± 0.38	-99.83 ± 0.50
Solvation phases			
$E_{\text{sol(GB)}}$	44.85 ± 0.22	27.56 ± 0.25	55.19 ± 0.31
E_{nonpolar}	-5.77 ± 0.02	-5.40 ± 0.03	-7.68 ± 0.02
$\Delta G_{\text{sol(GB)}}$	39.08 ± 0.22	22.16 ± 0.24	47.50 ± 0.30
$E_{\text{sol(PB)}}$	48.19 ± 0.26	29.41 ± 0.37	64.63 ± 0.37
E_{nonpolar}	-6.53 ± 0.01	-6.66 ± 0.03	-8.32 ± 0.02
$\Delta G_{\text{sol(PB)}}$	41.66 ± 0.25	22.75 ± 0.36	56.31 ± 0.36
Binding free energy			
$\Delta G_{\text{bind(GB)}}$	-43.29 ± 0.29	-29.59 ± 0.26	-52.33 ± 0.34
$\Delta G_{\text{bind(PB)}}$	-40.71 ± 0.33	-28.99 ± 0.40	-43.52 ± 0.42

inhibitor, which is relatively accessible to water molecules belongs to the complex $\text{DD9–}3\text{CL}^{\text{pro}} > \text{DD13–}3\text{CL}^{\text{pro}} > \text{0EN–}3\text{CL}^{\text{pro}}$ based on the total integration number. This data is also supported by the average value of SASA on the active site, which shows the same conclusion (Table S2†). This consideration was taken on the assumption that the more water molecules contained in the active site of the complex (SASA-active site), the greater the chance of water molecules interacting with the inhibitor. Investigation of the presence of water molecules at the active site of the complex provides a more comprehensive image of the effect of water solvent on molecular level interactions.

The binding affinity of inhibitor against the 3CL^{pro} enzyme

Determination of the binding affinity of each inhibitor to the 3CL^{pro} enzyme was calculated based on 100 frames extracted from the last 20 ns trajectories. The binding affinity calculation process uses the MM-PB/GBSA approach in the gas and solvent phases.⁵² The calculation process is showed in detail by considering several energy components described in Table 1. The calculation process for each energy component is the main

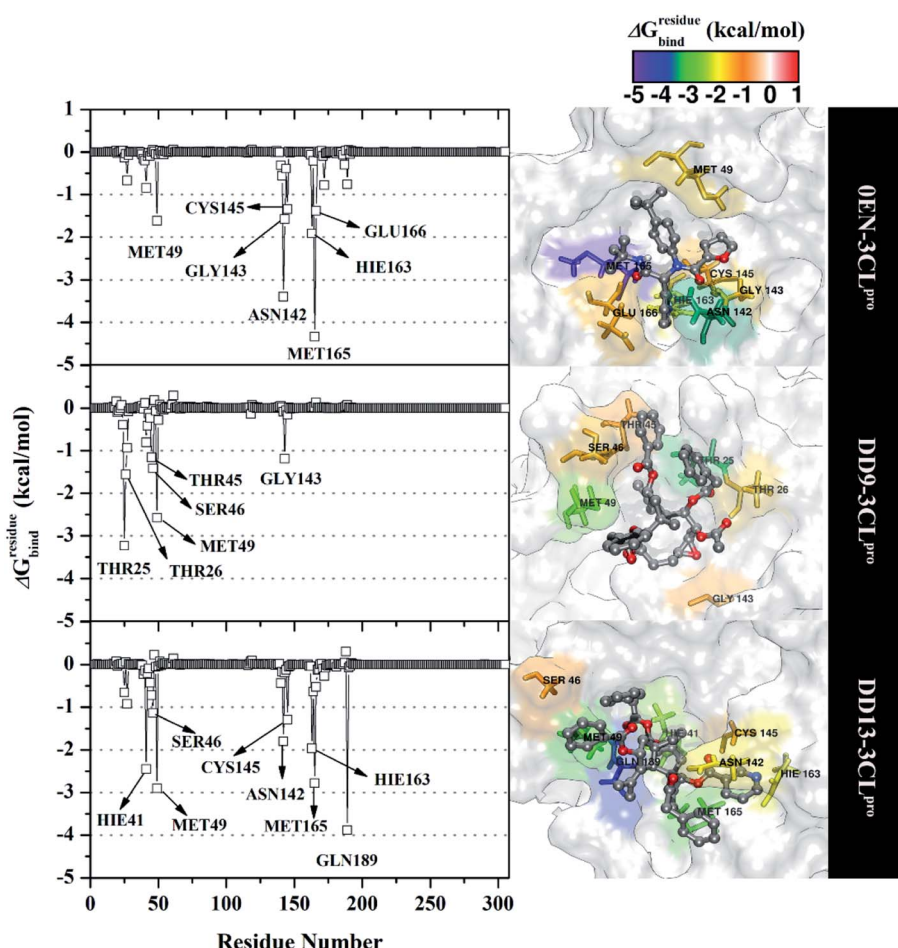


Fig. 6 The energy decomposition was calculated with the MM-GBSA approach. The results were plotted along with the simulation over the last 20 ns of each complex. It should be noted, Hie residue shows histidine (His) amino acid of receptor topology preparation using tleap that is available in the AMBER18 package.



focus to describe binding free energy (ΔG_{bind}). The energy component in the gas phase (ΔG_{gas}) shows that a good energy contribution is found in the van der Waals energy (E_{vdW}) compared to electrostatic energy (E_{ele}). On the other hand, the energy contribution to the solvent phase (ΔG_{sol}) shows a less favourable contribution to the polar energy for the Poisson Boltzmann/generalized Born model ($E_{\text{sol(PB)}}$) and $E_{\text{sol(GB)}}$). Centrally, this has an unfavourable impact on the affinity binding of the inhibitor-3CL^{pro}.

The contribution of each energy component provides a clear picture of the binding free energy. The DD13-3CL^{pro} complex showed promising ΔG_{bind} using the MM-GBSA and MM-PBSA approaches. It is taken from the consideration that DD13-3CL^{pro} ΔG_{bind} is smaller than 0EN-3CL^{pro} ΔG_{bind} as a reference. Thus, the candidate DD13 inhibitor has a promising potential in inhibiting the 3CL^{pro} enzyme. On the other hand, the DD9-3CL^{pro} complex showed a less favourable ΔG_{bind} because it had a higher ΔG_{bind} value than the 0EN-3CL^{pro} ΔG_{bind} value. It is caused by the contribution of E_{elec} , which is less favourable than the contribution of DD13 E_{elec} . Thus, the candidate DD9 is not recommended as an effective inhibitor of the 3CL^{pro} enzyme based on binding affinity calculation. Specifically, there are differences in the value of ΔG_{bind} in each approach. The results show that the MM-GBSA approach has a more favourable ΔG_{bind} value than the MM-PBSA approach. It is due to the unfavourable energy contribution of E_{sol} (solvation terms) from the Poisson Boltzmann model. Additionally, a recent study reports that the standard MM-PBSA may not be very accurate in the charged systems and needs to be modified to improve its calculation accuracy.^{53,54} However, the overall strength order of ΔG_{bind} using the MM-GBSA and MM-PBSA approaches showed the same trend towards each inhibitor, such as DD13-3CL^{pro} > 0EN-3CL^{pro} > DD9-3CL^{pro}. The candidate with a good binding affinity (higher negativity value) can bind strongly to the 3CL^{pro} enzyme subsite.⁵⁵ The goal is to inactivate the regulation of the main protease SARS-CoV-2 in the form of replication by blocking the active site of the 3CL^{pro} enzyme. More specifically, the process of inhibiting the main protease SARS-CoV-2 by inhibitors focuses on subsite binding pocket through interactions with amino acids.

Inhibitor-3CL^{pro} interaction in the binding pocket

The inhibition mechanism of the 3CL^{pro} enzyme was evaluated through the binding pattern of the inhibitor at the subsite binding pocket.⁵⁶ Some of the variables analysed in this section are energy decomposition, atom contacts, and hydrogen bonding. Energy decomposition was analysed using the MM-GBSA approach through 100 frames extracted from the last 20 ns trajectories. In detail, a per-residue analysis of the subsite binding showed that the van der Waals contact contributed to the inhibitor-3CL^{pro} interaction (Fig. S9†).

The calculation of energy decomposition, which is responsible for inhibitor-3CL^{pro} binding affinity shows that there are key residues on the subsite that play a crucial role in the inhibition mechanism of the 3CL^{pro} enzyme (Fig. 6). The evaluation process on amino acid residues that have a good binding

affinity with criteria for the value of $\Delta G_{\text{bind}}^{\text{residue}} \leq 1.00 \text{ kcal mol}^{-1}$.¹¹ Each complex showed several key residues (stronger binding affinity) found on the 3CL^{pro} enzyme subsite, such as 0EN-3CL^{pro}: seven key residues (S2: Met49, Met165, S1: Asn142, Gly143, Cys145, His163, and S3: Glu166), DD9-3CL^{pro}: six key residues (S2': Thr25, Thr26, S2: Thr45, Ser46, Met49, and S1: Gly163), and DD9-3CL^{pro}: eight key residues (S2: His41, Ser46, Met49, Met165, S1: Asn142, Cys145, His163, and S4: Gln189). These data suggest that the contribution of key residues in binding affinity inhibitor-3CL^{pro} plays a crucial role in the binding free energy of each complex. In particular, the candidate ligands show that the DD13 candidate has a good energy decomposition compared to the DD9 candidate. It can show in the number of key residues involved in direct interaction with candidate ligands. Especially, the DD13 inhibitor has more interaction with key residues compared to the DD9 inhibitor. In particular, Gln189 has a value: $-3.88 \text{ kcal mol}^{-1}$ with a strong binding affinity category. Additionally, His41 and Cys145 residues as catalytic centers are included in the key residues involved in the interaction with the DD13 inhibitor. Therefore, these data can explain why DD13 inhibitors have more promising free energy (ΔG_{bind}) than DD9 inhibitors

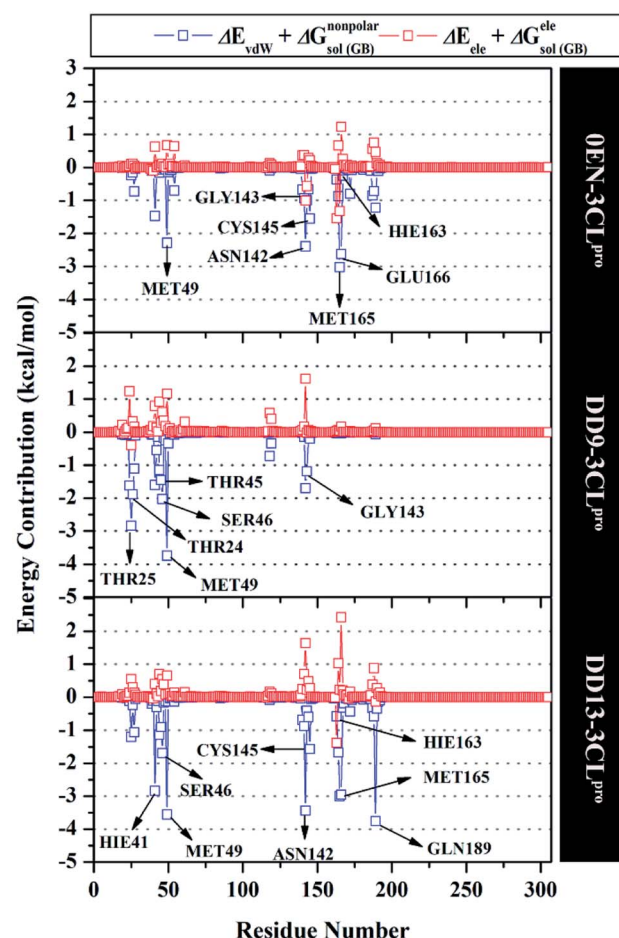


Fig. 7 Energy contribution from each residue of the 3CL^{pro} enzyme to the binding of each inhibitor.

(Table 1). More specifically, energy decomposition key residues are described in detail in the form of energy contributions to each complex. The energy contribution is described through the energy contribution in the gas and solvent phases, such as $\Delta E_{vdw} + \Delta G_{sol(GB)}^{nonpolar}$ and $\Delta E_{ele} + \Delta G_{sol(GB)}^{ele}$ (Fig. 7).

The atom contacts variable provides information to describe the inhibitor-3CL^{pro} interaction stability at the atomistic level.⁵⁷ The DD9 inhibitor had lower atom contacts with the amino acid residue on the active site of the 3CL^{pro} enzyme compared to the 0EN and DD13 inhibitors during the last 20 ns of simulation time (Fig. 8). These data can be seen in the average value of the atom contacts in each complex described in Table S2.[†] In contrast, the DD13 shows more intensive atom contacts with some of the key residues on the subsite binding pocket. Overall, the atom contacts of each inhibitor show 0EN-3CL^{pro}: 16 contacts, DD9-3CL^{pro}: 9 contacts, and DD13-3CL^{pro}: 20 contacts (Table S3[†]). Atom contacts that have occupation $\geq 80\%$ indicate a strong category. This further strengthens the assumption that DD13 candidate has a good interaction on the 3CL^{pro} subsite binding with more atom contacts.

More specifically, hydrogen bonding (H-bond) was calculated using the last 20 ns trajectories for each complex (Fig. 9). Hydrogen bonding plays a crucial role in inhibitor-receptor interactions.^{11,37,57,58} The analysis of the occupation of the H-bond played a major role in the evaluation of the inhibitor-3CL^{pro} interaction during the simulation time. The H-bond evaluation that has an occupancy value $\geq 80\%$ indicates

a strong category. In detail, the 0EN-3CL^{pro} interaction involves five H-bond: (i) O2 \cdots H-N(Glu166) at 89.55%, 2.90 Å, 159.22°, (ii) O1 \cdots H-N(Gly143) at 86.15%, 3.04 Å, 156.91°, (iii) N3 \cdots HE2-NE2(Hie163) at 82.50%, 3.02 Å, 141.92°, (iv) O1 \cdots HD22-ND2(Asn142) at 50.50%, 2.96 Å, 154.99°, and (v) O3 \cdots H-N(Gly143) at 29.50%, 3.27 Å, 129.45°. The H-bond results from the simulated MD showed consistent results with molecular docking as the initial reference (Fig. 1D). Meanwhile, the analysis results for candidate inhibitors showed three H-bond interactions for the DD9-3CL^{pro} complex: (i) O35 \cdots HD21-ND2(Asn142) at 5.20%, 3.01 Å, 149.09°, (ii) O32 \cdots HG-OG(Ser46) at 3.40%, 2.88 Å, 152.46°, and (iii) O35 \cdots HD22-ND2(Asn142) at 2.10%, 2.99 Å, 150.36°. Unfortunately, the three H-bonds show a weak category because they have a small H-bond occupancy (PHB < 10%). In contrast, the DD13-3CL^{pro} complex only involved one H-bond: N59 \cdots HE2-NE2(Hie163) at 88.85%, 3.09 Å, 147.28°. However, the hydrogen bond shows a good H-bond occupation with a strong bond category. It is because, during the H-bond simulation, 1777 frames out of 2000 total frames were recorded. Thus, this further strengthens the DD13 candidate to have a more dominant interaction than the DD9 candidate as an inhibitor.

Pharmacokinetic study of selected inhibitor

Based on several descriptions of molecular docking and MD simulation, the DD13 inhibitor is recommended as a selected candidate that has the potential to be an inhibitor of the SARS-CoV-2 main protease. The pharmacokinetic study aims to

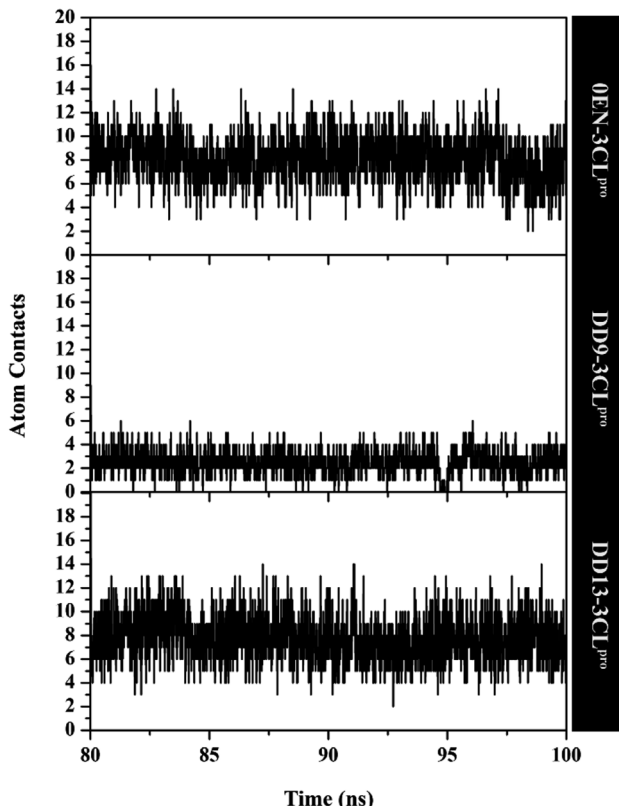


Fig. 8 Atom contacts of each inhibitor in complex with active site 3CL^{pro} enzyme.

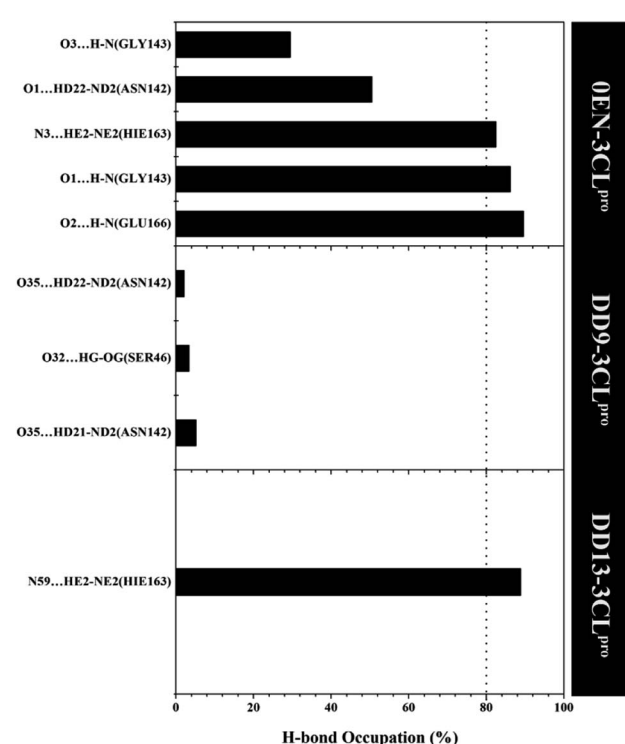


Fig. 9 The percentage of hydrogen bond over the last 20 ns trajectories (cut-off value: distance < 3.5 Å and angle $> 120^\circ$).



provide an initial prediction of the ADMET properties of the DD13 inhibitor (Table 2). One of them is the pkCSM server web service, which is widely applied to study the ADMET properties as a drug candidate.^{59–61}

Prediction results show that the candidate absorbed very well into the human small intestine (+HIA category). The predicted distribution of candidates does not cross the blood-brain barrier (–BBB). This indicates that the candidate does not interfere with the performance of the central nervous system.⁶⁰ Additionally, a crucial parameter such as the effect of the candidate on the body's metabolic processes showed that the candidate did not inhibit the activity of cytochrome isoenzymes (CYP), such as the CYP1A2, CYP2C19, CYP2C9, and CYP2D6. Toxicity prediction shows that the candidate is not toxic because the prediction results show promising results with the criteria of non-AMES toxicity and non-skin sensation. This information is a promising advantage of candidate properties to treat COVID-19 patients. However, the prediction results need to be tested in clinical trials. Hopefully, the prediction data in the ADMET properties study can be used as an initial reference in understanding the candidate's ability as a drug candidate.

Table 2 ADMET prediction of selected inhibitor using pkCSM server^a

Parameters	DD13
Absorption	
Caco-2 permeability (log Papp in 10^{-6} cm s ⁻¹)	1.20
Intestinal absorption-human (% absorbed)	100
Distribution	
BBB permeability (log BB)	-1.46
Metabolism	
CYP1A2 inhibitor	No
CYP2C19 inhibitor	No
CYP2C9 inhibitor	No
CYP2D6 inhibitor	No
Excretion	
Total clearance (log mL min ⁻¹ kg ⁻¹)	-0.093
Renal OCT2 substrate	No
Toxicity	
AMES toxicity	No
Skin sensitisation	No

^a High-Caco-2 permeability: log Papp > 0.90 and poor-Caco-2 permeability: log Papp < 0.90. Intestinal absorption-human (+): HIA > 30% and intestinal absorption-human (-): HIA < 30%. BBB permeability (+): log BB > 0.3 and BBB permeability (-): log BB < -1.0.

Conclusions

A combination of molecular docking and MD simulation is performed to study the interaction of dolabellane derivatives as the inhibitors of SARS-CoV-2 main protease. Determination of the active site using the selected sphere shows that the flexible conformation has good criteria with the RMSD pose of 1.39 Å. The molecular docking study showed that the DD9 and DD13 candidates showed a lower grid score than the native ligand. Meanwhile, the calculation of binding affinity using the MM-PB/GBSA approach showed that the DD13 candidate ΔG_{bind} showed more promising inhibition criteria for the 3CL^{pro} enzyme than the DD9 candidate. This result was strengthened by the interaction of the DD13 on the subsite binding pocket of the 3CL^{pro} enzyme. Evaluation of energy decomposition showed that residue Hie41 and Cys145 had strong binding affinity interactions with the DD13 candidate. Besides, the H-bond analysis of the DD13 candidate with Hie163 residue showed a strong category with 88.85% occupation. Furthermore, the DD13 candidate showed promising ADMET properties criteria as a drug candidate with criteria +HIA, -BBB, non-inhibitor of cytochrome isoenzymes, and non-toxic.

Conflicts of interest

The authors declare no conflict of interest.

References

- 1 G. Vargas, L. H. Medeiros Geraldo, N. Gedeão Salomão, M. Viana Paes, F. Regina Souza Lima and F. Carvalho Alcantara Gomes, *Brain Behav. Immun. Health.*, 2020, **7**, 100127.
- 2 B. Hu, H. Guo, P. Zhou and Z. L. Shi, *Nat. Rev. Microbiol.*, 2021, **19**, 141–154.
- 3 Y. Chen, Q. Liu and D. Guo, *J. Med. Virol.*, 2020, **92**, 418–423.
- 4 R. Lu, X. Zhao, J. Li, P. Niu, B. Yang, H. Wu, W. Wang, H. Song, B. Huang, N. Zhu, Y. Bi, X. Ma, F. Zhan, L. Wang, T. Hu, H. Zhou, Z. Hu, W. Zhou, L. Zhao, J. Chen, Y. Meng, J. Wang, Y. Lin, J. Yuan, Z. Xie, J. Ma, W. J. Liu, D. Wang, W. Xu, E. C. Holmes, G. F. Gao, G. Wu, W. Chen, W. Shi and W. Tan, *Lancet*, 2020, **395**, 565–574.
- 5 Y. Tan, S. G. Lim and W. Hong, *Antiviral Res.*, 2005, **65**, 69–78.
- 6 M. Miczi, M. Golda, B. Kunkli, T. Nagy, J. Tőzsér and J. A. Mótyán, *Int. J. Mol. Sci.*, 2020, **21**, 1–19.
- 7 W. Vuong, M. B. Khan, C. Fischer, E. Arutyunova, T. Lamer, J. Shields, H. A. Saffran, R. T. McKay, M. J. van Belkum, M. A. Joyce, H. S. Young, D. L. Tyrrell, J. C. Vederas and M. J. Lemieux, *Nat. Commun.*, 2020, **11**, 1–8.
- 8 V. Mody, J. Ho, S. Wills, A. Mawri, L. Lawson, M. C. C. J. C. Ebert, G. M. Fortin, S. Rayalam and S. Taval, *Commun. Biol.*, 2021, **4**, 1–10.
- 9 Z. Jin, Y. Zhao, Y. Sun, B. Zhang, H. Wang, Y. Wu, Y. Zhu, C. Zhu, T. Hu, X. Du, Y. Duan, J. Yu, X. Yang, X. Yang, K. Yang, X. Liu, L. W. Guddat, G. Xiao, L. Zhang, H. Yang and Z. Rao, *Nat. Struct. Mol. Biol.*, 2020, **27**, 529–532.



10 J. C. Ferreira, S. Fadl, A. J. Villanueva and W. M. Rabeh, *Front. Chem.*, 2021, **9**, 1–11.

11 B. Nutho, P. Mahalapbutr, K. Hengphasatporn, N. C. Pattranggoon, N. Simanon, Y. Shigeta, S. Hannongbua and T. Rungrotmongkol, *Biochemistry*, 2020, **59**, 1769–1779.

12 G. J. Lockbaum, A. C. Reyes, J. M. Lee, R. Tilwawala, E. A. Nalivaika, A. Ali, N. K. Yilmaz, P. R. Thompson and C. A. Schiffer, *Viruses*, 2021, **13**, 174.

13 A. Gahlawat, N. Kumar, R. Kumar, H. Sandhu, I. P. Singh, S. Singh, A. Sjöstedt and P. Garg, *J. Chem. Inf. Model.*, 2020, **60**, 5781–5793.

14 H. M. Mengist, T. Dilnessa and T. Jin, *Front. Chem.*, 2021, **9**, 1–19.

15 Purwati, A. Miatmoko, Nasronudin, E. Hendrianto, D. Karsari, A. Dinaryanti, N. Ertanti, I. S. Ihsan, D. S. Purnama, T. P. Asmarawati, E. Marfiani, Yulistiani, A. N. Rosyid, P. A. Wulaningrum, H. W. Setiawan, I. Siswanto and N. N. T. Puspaningsih, *PLoS One*, 2021, **16**, 1–27.

16 Z. Li, X. Li, Y. Y. Huang, Y. Wu, R. Liu, L. Zhou, Y. Lin, D. Wu, L. Zhang, H. Liu, X. Xu, K. Yu, Y. Zhang, J. Cui, C. G. Zhan, X. Wang and H. Bin Luo, *Proc. Natl. Acad. Sci. U. S. A.*, 2020, **117**, 27381–27387.

17 S. H. Ghoran, M. El-shazly, N. Sekeroglu and A. Kijjoa, *Molecules*, 2021, **26**, 1754.

18 M. Omrani, M. Keshavarz, S. Nejad Ebrahimi, M. Mehrabi, L. J. McGaw, M. Ali Abdalla and P. Mehrbod, *Front. Pharmacol.*, 2021, **11**, 2115.

19 A. D. S. Antonio, L. S. M. Wiedemann and V. F. Veiga-Junior, *RSC Adv.*, 2020, **10**, 23379–23393.

20 A. P. Wardana, N. S. Aminah, M. Rosyda, M. I. Abdjan, A. N. Kristanti, K. N. W. Tun, M. I. Choudhary and Y. Takaya, *Heliyon*, 2021, **7**, 1–14.

21 C. C. Wen, Y. H. Kuo, J. T. Jan, P. H. Liang, S. Y. Wang, H. G. Liu, C. K. Lee, S. T. Chang, C. J. Kuo, S. S. Lee, C. C. Hou, P. W. Hsiao, S. C. Chien, L. F. Shyur and N. S. Yang, *J. Med. Chem.*, 2007, **50**, 4087–4095.

22 M. A. A. Ibrahim, A. H. M. Abdelrahman, M. A. M. Atia, T. A. Mohamed, M. F. Moustafa, A. R. Hakami, S. A. M. Khalifa, F. A. Alhumaydhi, F. Alrumaihi, S. H. Abidi, K. S. Allemailem, T. Efferth, M. E. Soliman, P. W. Paré, H. R. El-Seedi and M. E. F. Hegazy, *Mar. Drugs*, 2021, **19**, 391.

23 L. Santacruz, D. X. Hurtado, R. Doohan, O. P. Thomas, M. Puyana and E. Tello, *Sci. Rep.*, 2020, **10**, 1–11.

24 K. Ogawa, S. Nakamura, K. Hosokawa, H. Ishimaru, N. Saito, K. Ryu, M. Fujimuro, S. Nakashima and H. Matsuda, *J. Nat. Med.*, 2018, **72**, 439–447.

25 A. Pardo-Vargas, F. A. Ramos, C. C. Cirne-Santos, P. R. Stephens, I. C. P. Paixão, V. L. Teixeira and L. Castellanos, *Bioorg. Med. Chem. Lett.*, 2014, **24**, 4381–4383.

26 N. Rahman, Z. Basharat, M. Yousuf, G. Castaldo, L. Rastrelli and H. Khan, *Molecules*, 2020, **2**, 1–12.

27 T. L. Augustin, R. Hajbabaie, M. T. Harper and T. Rahman, *Molecules*, 2020, **25**, 5501.

28 I. A. Guedes, L. S. C. Costa, K. B. dos Santos, A. L. M. Karl, G. K. Rocha, I. M. Teixeira, M. M. Galheigo, V. Medeiros, E. Krempser, F. L. Custódio, H. J. C. Barbosa, M. F. Nicolás and L. E. Dardenne, *Sci. Rep.*, 2021, **11**, 1–20.

29 C. H. Zhang, E. A. Stone, M. Deshmukh, J. A. Ippolito, M. M. Ghahremanpour, J. Tirado-Rives, K. A. Spasov, S. Zhang, Y. Takeo, S. N. Kudalkar, Z. Liang, F. Isaacs, B. Lindenbach, S. J. Miller, K. S. Anderson and W. L. Jorgensen, *ACS Cent. Sci.*, 2021, **7**, 467–475.

30 D. El Ahdab, L. Lagardère, T. J. Inizan, F. Célerse, C. Liu, O. Adjoua, L. H. Jolly, N. Gresh, Z. Hobaika, P. Ren, R. G. Maroun and J. P. Piquemal, *J. Phys. Chem. Lett.*, 2021, **12**, 6218–6226.

31 T. Jaffrelot Inizan, F. Célerse, O. Adjoua, D. El Ahdab, L. H. Jolly, C. Liu, P. Ren, M. Montes, N. Lagarde, L. Lagardère, P. Monmarché and J. P. Piquemal, *Chem. Sci.*, 2021, **12**, 4889–4907.

32 M. J. Frisch, G. W. Trucks, H. B. Schlegel, G. E. Scuseria, M. A. Robb, J. R. Cheeseman, G. Scalmani, V. Barone, B. Mennucci, G. A. Petersson, H. Nakatsuji, M. Caricato, X. Li, H. P. Hratchian, A. F. Izmaylov, J. Bloino, G. Zheng, J. L. Sonnenberg, M. Hada, M. Ehara, K. Toyota, R. Fukuda, J. Hasegawa, M. Ishida, T. Nakajima, Y. Honda, O. Kitao, H. Nakai, T. Vreven, J. A. Montgomery Jr, J. E. Peralta, F. Ogliaro, M. Bearpark, J. J. Heyd, E. Brothers, K. N. Kudin, V. N. Staroverov, R. Kobayashi, J. Normand, K. Raghavachari, A. Rendell, J. C. Burant, S. S. Iyengar, J. Tomasi, M. Cossi, N. Rega, J. M. Millam, M. Klene, J. E. Knox, J. B. Cross, V. Bakken, C. Adamo, J. Jaramillo, R. Gomperts, R. E. Stratmann, O. Yazyev, A. J. Austin, R. Cammi, C. Pomelli, J. W. Ochterski, R. L. Martin, K. Morokuma, V. G. Zakrzewski, G. A. Voth, P. Salvador, J. J. Dannenberg, S. Dapprich, A. D. Daniels, O. Farkas, J. B. Foresman, J. V. Ortiz, J. Cioslowski, and D. J. Fox, *Gaussian 16, Revision C.01*, Gaussian, Inc., Wallingford CT, 2016.

33 S. R. Brozell, S. Mukherjee, T. E. Balias, D. R. Roe, D. A. Case and R. C. Rizzo, *J. Comput.-Aided Mol. Des.*, 2012, **26**, 749–773.

34 K. Liu and H. Kokubo, *J. Comput.-Aided Mol. Des.*, 2020, **34**, 1195–1205.

35 J. Wang, R. M. Wolf, J. W. Caldwell, P. A. Kollman and D. A. Case, *J. Comput. Chem.*, 2004, **25**, 1157–1174.

36 D. R. Roe and T. E. Cheatham, *J. Chem. Theory Comput.*, 2013, **9**, 3084–3095.

37 D. Mishra, R. R. Maurya, K. Kumar, N. S. Munjal, V. Bahadur, S. Sharma, P. Singh and I. Bahadur, *J. Mol. Liq.*, 2021, **335**, 116185.

38 B. R. Miller, T. D. McGee, J. M. Swails, N. Homeyer, H. Gohlke and A. E. Roitberg, *J. Chem. Theory Comput.*, 2012, **8**, 3314–3321.

39 H. Luo, D. F. Liang, M. Y. Bao, R. Sun, Y. Y. Li, J. Z. Li, X. Wang, K. M. Lu and J. K. Bao, *Int. J. Oral Sci.*, 2017, **9**, 53–62.

40 D. E. V. Pires, T. L. Blundell and D. B. Ascher, *J. Med. Chem.*, 2015, **58**, 4066–4072.



41 W. J. Allen, T. E. Balias, S. Mukherjee, S. R. Brozell, D. T. Moustakas, P. T. Lang, D. A. Case, I. D. Kuntz and R. C. Rizzo, *J. Comput. Chem.*, 2015, **36**, 1132–1156.

42 J. He, L. Hu, X. Huang, C. Wang, Z. Zhang, Y. Wang, D. Zhang and W. Ye, *Int. J. Antimicrob. Agents*, 2020, **56**, 106055.

43 Y. Kumar, H. Singh and C. N. Patel, *J. Infect. Public Health*, 2020, **13**, 1210–1223.

44 A. Kumari, V. S. Rajput, P. Nagpal, H. Kukrety, S. Grover and A. Grover, *J. Biomol. Struct. Dyn.*, 2020, 1–13.

45 J. Tan, K. H. G. Verschueren, K. Anand, J. Shen, M. Yang, Y. Xu, Z. Rao, J. Bigalke, B. Heisen, J. R. Mesters, K. Chen, X. Shen, H. Jiang and R. Hilgenfeld, *J. Mol. Biol.*, 2005, **354**, 25–40.

46 M. E. Abouelela, H. K. Assaf, R. A. Abdelhamid, E. S. Elkhyat, A. M. Sayed, T. Oszako, L. Belbahri, A. E. El Zowalaty and M. S. A. Abdelkader, *Molecules*, 2021, **26**, 1767.

47 A. Bornot, C. Etchebest and A. G. De Brevern, *Proteins: Struct., Funct., Bioinf.*, 2011, **79**, 839–852.

48 J. Lee, L. J. Worrall, M. Vuckovic, F. I. Rosell, F. Gentile, A. T. Ton, N. A. Caveney, F. Ban, A. Cherkasov, M. Paetzel and N. C. J. Strynadka, *Nat. Commun.*, 2020, **11**, 1–9.

49 D. Suárez and N. Díaz, *J. Chem. Inf. Model.*, 2020, **60**, 5815–5831.

50 N. Ansari, V. Rizzi, P. Carloni and M. Parrinello, *J. Am. Chem. Soc.*, 2021, **143**, 12930–12934.

51 B. Nutho, S. Pengthaisong, A. Tankrathok, V. S. Lee, J. R. K. Cairns, T. Rungrotmongkol and S. Hannongbua, *Biomolecules*, 2020, **10**, 1–19.

52 C. Wang, D. Greene, L. Xiao, R. Qi and R. Luo, *Front. Mol. Biosci.*, 2018, **4**, 1–18.

53 H. M. Ding, Y. W. Yin, S. Di Ni, Y. J. Sheng and Y. Q. Ma, *Chin. Phys. Lett.*, 2021, **38**, 018701.

54 Y. J. Sheng, Y. W. Yin, Y. Q. Ma and H. M. Ding, *J. Chem. Inf. Model.*, 2021, **61**, 2454–2462.

55 M. I. Choudhary, M. Shaikh, A.-T. Wahab and A.-U. Rahman, *PLoS One*, 2020, **15**, 1–15.

56 Y. L. Weng, S. R. Naik, N. Dingelstad, M. R. Lugo, S. Kalyaanamoorthy and A. Ganesan, *Sci. Rep.*, 2021, **11**, 1–22.

57 T. Somboon, P. Mahalapbutr, K. Sanachai, P. Maitarad, V. S. Lee and T. Rungrotmongkol, *J. Mol. Liq.*, 2020, **322**, 114999.

58 S. Ahmad, Y. Waheed, S. Ismail, S. Bhatti, S. W. Abbasi and K. Muhammad, *Molecules*, 2021, **26**, 1446.

59 M. A. Guimarães, R. N. De Oliveira, R. L. De Almeida, A. C. Mafud, A. L. V. Sarkis, R. Ganassin, M. P. Da Silva, D. B. Roquini, L. M. Veras, T. C. H. Sawada, C. D. Ropke, L. A. Muehlmann, G. A. Joanitti, S. A. S. Kuckelhaus, S. M. Allegretti, Y. P. Mascarenhas, J. de Moraes and J. R. S. A. Leite, *PLoS One*, 2018, **13**, 1–19.

60 Y. Han, J. Zhang, C. Q. Hu, X. Zhang, B. Ma and P. Zhang, *Front. Pharmacol.*, 2019, **10**, 1–12.

61 A. Mohammad, E. Alshawaf, S. K. Marafie, M. Abu-Farha, F. Al-Mulla and J. Abubaker, *Biomolecules*, 2021, **11**, 573.

